J. Fluid Mech. (2022), *vol*. 935, A42, doi:10.1017/jfm.2022.54

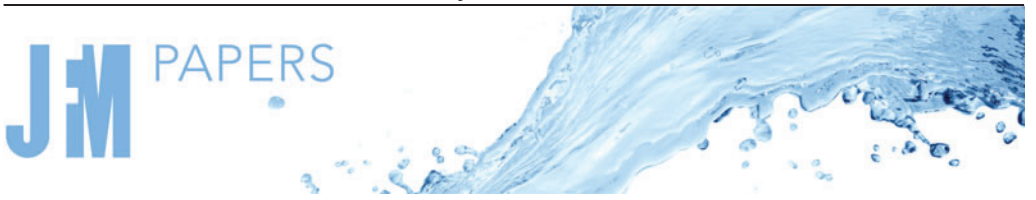

Wall similarity in turbulent boundary layers over wind waves

Meital Geva[1],† **and Lev Shemer**[1]

[1]School of Mechanical Engineering, Tel-Aviv University, Tel-Aviv 69978, Israel

(Received 24 August 2021; revised 9 December 2021; accepted 17 January 2022)

The structure of the steady boundary layer in the airflow over young wind waves is studied in detail using extensive data accumulated in our laboratory as well as in additional laboratory facilities and in field measurements. Following the approach adopted in studies of turbulent flow over solid rough surfaces, the coupling between the spatial evolution of wind waves and wind velocity profiles over the water is analysed. The roughness of the moving water surface under wind is not constant; wind waves that constitute the roughness elements are unsteady, random and three-dimensional. The effective water surface roughness increases with airflow velocity as well as with downstream distance. Nevertheless, the existence of wall similarity as observed in a flow over solid surfaces is demonstrated; a fully rough boundary layer is obtained for young wind waves at diverse operational conditions. This approach enables quantitative study of the coupling between the airflow and local wind wave characteristics.

Key words: wind–wave interactions, turbulent boundary layers

1. Introduction

The process of excitation of waves on the water surface by wind has remained the focus of extensive studies for many decades. However, the details of momentum and energy transfer from the airflow to the growing waves, as well as the reverse effect of waves on the evolution of the wind velocity profile over the wavy water surface, are not yet known in sufficient detail. The water surface in the presence of wind waves is highly irregular and three-dimensional; even for steady wind forcing, its statistical properties vary along the airflow (Mitsuyasu 1970; Shemer 2019). Accurate description of the air velocity profile above wind waves is the key for understanding the exchange of momentum, energy and mass at the air–water interface. It is generally accepted that similar to airflow over solid rough surfaces, the wind velocity over waves has a logarithmic dependence on the elevation over the mean water surface z, see Neumann (1956) and additional

† Email address for correspondence: meitalgeva@mail.tau.ac.il

references therein. The mean wind profile that is extensively used in field, laboratory and numerical wind waves studies,

$$U(z) = \frac{u_*}{\kappa} \ln\left(\frac{z}{z_0}\right), \tag{1.1}$$

depends on two parameters that have to be evaluated from the experimental data. Here $\kappa = 0.41$ is the von Kármán constant; and the friction velocity u_* together with the air density ρ define the wind stress $\tau = \rho u_*^2$ at the air–water interface. The effective roughness parameter z_0 suggested by Prandtl (1932) is a complicated function of the roughness density; it cannot be directly measured and related to the geometrical height of the roughness elements (Donelan *et al.* 1993; Csanady 2001). Based on dimensional reasoning, Charnock (1955) proposed the following expression:

$$\alpha_{Ch} = \frac{z_0 g}{u_*^2} = \text{const.}, \tag{1.2}$$

where g is the gravity acceleration. Charnock suggested the value of $\alpha_{Ch} = 0.007$. However, the range of variation of α_{Ch} documented in the literature covers approximately two orders of magnitude (Wu 1969; Janssen 2008; Bye, Ghantous & Wolff 2010). Liberzon & Shemer (2011) attempted to estimate α_{Ch} for very young wind waves in a laboratory facility by measuring detailed velocity profiles. They found that α_{Ch} depends on the fetch and on the wind velocity and varies from 0.001 to approximately 0.011. In field measurement, the roughness coefficient is often estimated based on a velocity measurement at a single elevation over the water surface, $z = 10$ m, which is denoted as U_{10}. For a developed sea, the routinely adopted value is $\alpha_{Ch} \approx 0.01$ (Smith 1980). Yet, Janssen (1989) used $\alpha_{Ch} = 0.0065$, Massel (1996) suggested $\alpha_{Ch} = 0.11$, while Young (1999) reported a different and somewhat narrower range of $0.014 \leqslant \alpha_{Ch} \leqslant 0.035$. Additional values of α_{Ch} are documented by Bye & Wolff (2008), Peña & Gryning (2008) and references therein. The roughness parameter z_0 varies with fetch and with wind conditions. Owing to its importance in defining the air profile (1.1), there is an ongoing attempt to relate z_0 with diverse wave characteristics such as the significant wave height H_s and the inverse wave age u_*/c_p, where c_p is the phase velocity of the water wave at the peak frequency in the spectrum, (Toba *et al.* 1990; Massel 1996; Taylor & Yelland 2001; Toba, Smith & Ebuchi 2001; Bye & Wolff 2008). Nevertheless, the dependence of the surface roughness on sea state remains controversial (Taylor & Yelland 2001; Drennan, Taylor & Yelland 2005).

The considerable scatter in the reported values of α_{Ch} stems partially from the fact that in field measurements, the roughness coefficient is routinely estimated based on velocity measurement at a single elevation over the water surface. This is because measuring the exact vertical velocity profiles in field conditions is challenging, in part owing to the variation in wind direction and strength. The use of several anemometers enables a limited vertical resolution at a fixed fetch (Mitsuyasu 1969; Hristov, Miller & Friehe 2003; Li *et al.* 2020). In recent years, scanning techniques are sometimes used to determine the whole velocity profile simultaneously. These measurements have insufficient spatial resolution; they are usually not related to wind wave studies (Pichugina *et al.* 2012). Measurements of airflow profiles in wind wave laboratory facilities, while performed under controlled conditions and are more accurate than the field data, also have limited spatial resolution (Mitsuyasu & Honda 1974, 1982; Mitsuyasu & Rikiishi 1978; Kawamura *et al.* 1981; Hsu *et al.* 1982; Kawamura & Toba 1988; Tseng, Hsu & Wu 1992; Caulliez, Makin & Kudryavtsev 2008). Kawamura *et al.* (1981) and (Toba 1988) provided evidence

of a probable boundary layer similarity in air. Kawamura & Toba (1988) visualized large-scale ordered turbulent motions in the airflow that corresponds to the wavelengths of the underlying wind waves. Longo *et al.* (2012) analysed extensively the Reynolds stresses both in air and water. However, this study was performed in a short tank (less than 1 m long) at a single wind forcing. Zavadsky & Shemer (2012) performed extensive high-resolution measurements of velocity profiles above wind waves at various wind strengths and at different locations along the test sections. The Reynolds stresses where measured as well and used to obtain independent estimates of the friction velocities that agreed well with the values of u_* derived by fitting the velocity records to log-profiles. Zavadsky & Shemer (2012) found that for a given wind forcing, the friction velocity remains almost unchanged along the test section, although the boundary layer spatially evolves. This finding was also reported in additional studies in wind wave facilities (Plant & Wright 1977; Mitsuyasu & Rikiishi 1978; Hsu *et al.* 1982; Caulliez *et al.* 2008). High-resolution particle image velocimetry (PIV) air velocity measurements in the close vicinity of the interface at a single location along the test section were performed by Buckley, Veron & Yousefi (2020).

The information on the airflow over the moving spatially developing wind waves is thus limited. Nonetheless, extensive literature exists on velocity profiles over smooth and rough solid surfaces. For recent summaries of those studies, see e.g. Chung *et al.* (2021), Nugroho *et al.* (2021) and additional references therein. It is generally accepted that the turbulent boundary layer of a smooth surface can be divided into the inner layer dominated by viscosity, outer layer dominated by turbulent Reynolds stresses and the overlap region where both momentum transfer mechanisms are essential. In recent decades, the effect of wall roughness on mean turbulent flow over a solid surface, initially discovered by Nikuradse (1950), has attained renewed attention in free and bounded flows (see Jimenez 2004; Shockling, Allen & Smits 2006; Schultz & Flack 2007; Flack, Schultz & Barros 2020 and additional references therein). Those detailed studies of the turbulent flow structure indicated that when the roughness effects are limited to the flow within the near-wall region, the outer flow is practically independent of the surface conditions. The mean turbulent velocity profile in the overlap and outer layer is thus unaffected by the roughness and exhibits wall similarity (Flack & Schultz 2014). The effect of rough surface topography on the boundary layer structure was reviewed by Chung *et al.* (2021).

In spite of essential differences in the shape of the moving and evolving air–water interface and the rigid homogeneous rough solid surface, we show that there is an essential similarity between the airflow profiles in both cases. We investigate the mutual influence of airflow and wind waves using extensive data accumulated in our laboratory. The spatial variation of the boundary layer characteristics are integrated with water surface features that exhibit modifications in space, as reported by Zavadsky & Shemer (2017*a*,*b*) and Shemer, Singh & Chernyshova (2020). Examination of the measured spatial variation of the airflow and of the wind wave field from this perspective enables a new insight into the coupling of wind and waves.

2. Characterization of the principal features of the wavy water surface in our experimental facility

Measurements were performed at the Tel-Aviv University wind wave facility that consists of a closed-loop wind tunnel installed atop of a 5 m long rectangular test section. The test section is 0.4 m wide and 0.5 m high and is filled with water to a depth of 0.19 m. The maximum wind velocity in the test section supplied by a computer-controlled blower exceeds 12 m s^{-1}. Large settling chambers (approximately 1 m^3) are positioned at the inlet and the exit of the test section. The air from the inlet settling chamber flows through

a honeycomb and a converging nozzle with an area reduction ratio of approximately 4 to the test section; a flexible 40-cm-long flap connects the bottom of the nozzle to the test section slightly above the mean water level height to ensure a smooth uniform airflow. An instrument carriage that supports the wave gauges and airflow sensors can be positioned at any fetch x. The wave and the airflow sensors are mounted on separate vertical precision stages with a positioning accuracy of 0.05 mm. A Pitot tube with an outer diameter of 1 mm measures the mean airflow velocity profile, while an X-hot film probe is used to determine the vertical profiles of the turbulent air velocity fluctuations in the horizontal, u', and the vertical, w', directions, as well as the mean Reynolds stresses $\overline{u'w'}$. To provide reliable data, both the X-hot film and the Pitot tube need to remain dry. To eliminate their wetting, a maximum wave height detector located at a fixed vertical displacement below the sensitive air sensors was used. A special iterative procedure allowed for the estimation of the maximum possible crest height at each location and at each wind velocity. Multiple capacitance-type wave gauges mounted on a horizontal bar were used to measure the instantaneous surface elevation η at several axial locations simultaneously. All measurements were performed along the centreline of the test section. These detailed and time-consuming measurements were possible because all experiments were run autonomously without human intervention, with a single computer controlling the wind speed in the tunnel, the probe calibration and the vertical positioning of all sensors. The data acquisition lasted from a few minutes for wind velocity measurements at each point to an hour or more for surface elevation variation. A heat exchanger in the wind-tunnel maintained a constant air temperature during the whole experiment. The acquisition duration was thus larger by orders of magnitude than the characteristic wind wave periods that range from 0.1 s to 1.5 s. More information about the experimental facility and procedure is given in Liberzon & Shemer (2011) and Zavadsky & Shemer (2012).

Measurements of airflow over a randomly moving water surface even at a single downstream location x and wind velocity thus require a demanding experimental procedure. Unlike the flow over a solid rough surface that is usually statistically homogeneous, the spatial variability of the statistical parameters of the wind wave field further complicates measurements in the airflow boundary layer over wind waves. Wind wave evolution with fetch prescribes the topography of the water surface. Waves under the action of steady wind are essentially three-dimensional and random, losing their coherence quickly in time as well as in space (Zavadsky, Benetazzo & Shemer 2017; Shemer & Singh 2021). Zavadsky, Liberzon & Shemer (2013) and Zavadsky & Shemer (2017*a*) demonstrated that the characteristic wave amplitude represented by the root mean square (r.m.s.) of the surface elevation variations around the mean value, $\eta_{rms} = \overline{\eta^2}^{1/2}$, growth with the fetch x. The wave amplitude growth, however, is accompanied by increase in the peak wavelength λ_p, so that the characteristic steepness $\epsilon = \eta_{rms} k_p$, where the peak wavenumber $k_p = 2\pi/\lambda_p$ remains approximately constant, $\epsilon \approx 0.2$, only slightly increasing with fetch x and wind velocity. The steepness never exceeds notably $\epsilon \approx 0.25$ as a result of wave breaking. These results are consistent with the values given by Hsu *et al.* (1982) and Buckley *et al.* (2020). As the crests of nonlinear water waves are larger than the troughs, the skewness of the surface elevation, $c_3 = \overline{\eta^3}/\overline{\eta^2}^{3/2}$, is always positive, increasing from $c_3 \approx 0.07$ at very short fetches and weak winds, to maximum values of $c_3 \approx 0.45$ for strong winds and large values of x. The kurtosis $c_4 = \overline{\eta^4}/\overline{\eta^2}^2$ is somewhat below the value of 3, thus indicating that the tail in the probability distribution of η for the young wind waves is shorter than that in the Gaussian distribution.

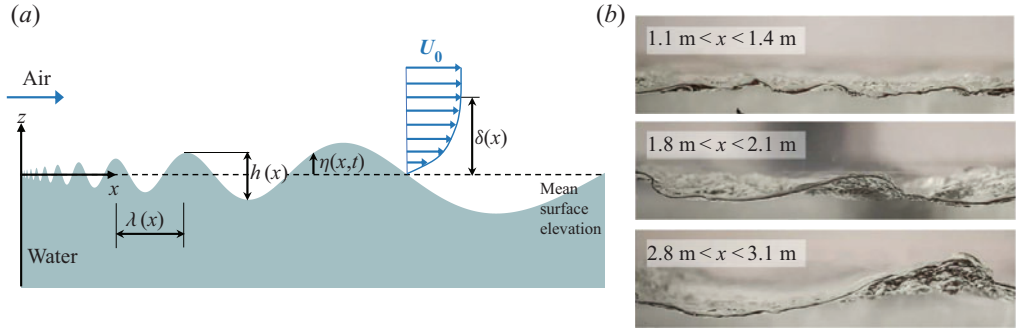

Figure 1. (*a*) Schematic illustration of wind waves growth and the developing boundary layer in air; (*b*) snapshots of the wave field taken through the side window of the test section at three locations; the maximum velocity $U_0 = 11.2$ m s^{-1}.

U_0 (m s^{-1})	$u_{*,ZS}$ (m s^{-1})	$u_{*,MI}$ (m s^{-1})	$U_{10,ZS}$ (m s^{-1})
5.5	0.29	0.30 ± 0.009	8.75
6.6	0.37	0.39 ± 0.011	10.6
7.7	0.45	0.47 ± 0.012	13.0
8.9	0.56	0.54 ± 0.013	15.3
10.05	0.68	0.61 ± 0.011	17.7
11.2	0.85	0.77 ± 0.014	21.5

Table 1. Characteristic mean wind velocities: U_0, the maximum wind velocity; u_*, the friction velocity; U_{10}, the estimated wind velocity at $z = 10$ m (1.1). Here the subscripts ZS and MI refer to Zavadsky & Shemer (2012) and to the momentum integral (Appendix A).

3. Evolution of wind waves and of wind velocity profiles with fetch

Both the longitudinal scale of wind waves (wavelength λ) and the corresponding vertical scale, the wave height h, grow under steady wind forcing with fetch x, as is presented schematically in figure 1(*a*); variation of wave parameters with fetch is clearly visible in figure 1(*b*). It is important to note that the simplified two-dimensional illustration in figure 1(*a*) does not fully depict real wind waves that are essentially random and three-dimensional, as seen in the snapshots. The vertical scale of wind waves may be presented by the characteristic r.m.s. surface elevation $(\overline{\eta(x)^2})^{1/2}$ computed as the time average of the measured variation in time of the surface elevation $\eta(t)$ relative the mean water level.

Velocity profiles were measured at multiple elevations above the mean water surface level at seven fetches in the range 1 m $\leqslant x \leqslant$ 3.4 m and at six wind velocities. The mean wind velocities derived from profiles $U(z)$ are listed in table 1. For any given blower setting, the maximum wind velocities U_0 remained practically constant along the whole test section. In Zavadsky & Shemer (2012), the values of u_* were extracted by two independent methods, from the measured mean turbulent velocity profile in the inner part of the boundary layer above the wavy water surface and from the Reynolds shear stresses. Estimates based on the two approaches agreed well and demonstrated that for a given airflow rate, the variation of u_* with fetch did not exceed approximately 7 %. The mean values of the friction velocities obtained in Zavadsky & Shemer (2012) for a given air flow forcing are referred to as $u_{*,ZS}$ in table 1. Additional independent evaluation of

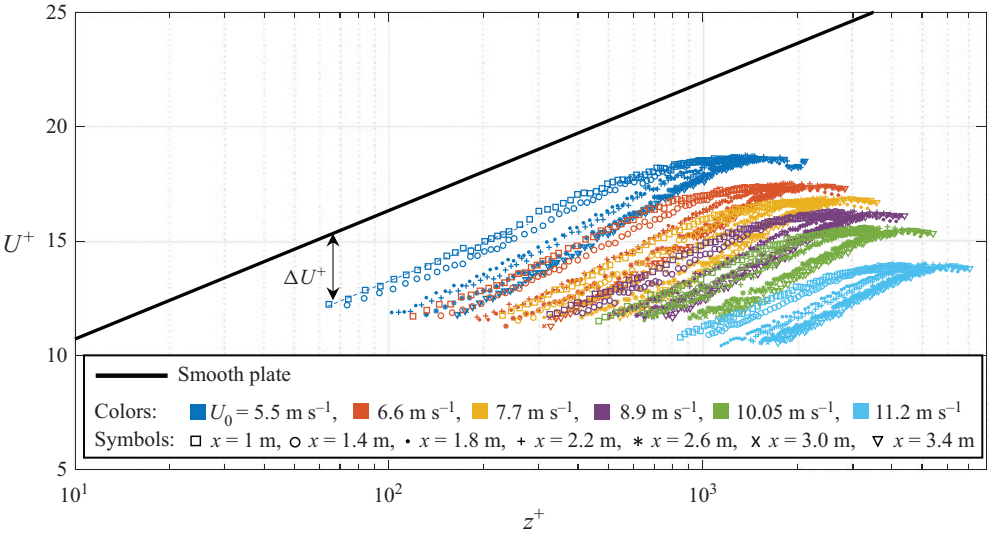

Figure 2. Dimensionless mean velocity profiles at various wind velocities and fetches.

u_* was performed based on the boundary layer momentum integral equation, for details see Appendix A. Those values are referred to as $u_{*,MI}$ and mostly agree well with the estimates based on Zavadsky & Shemer (2012). The somewhat higher values of $u_{*,ZS}$ may be attributed to an unavoidable overestimate of the friction velocity in the presence of high amplitude waves owing to the insertion of some portion of the wake in the fit. The integral method is more robust and less sensitive to the profile details in the lower part of the boundary layer; it thus indeed yields lower values of u_* at those conditions. In the following, for each U_0, the average values of u_* presented in the two columns of table 1 are used.

The dimensionless profiles are plotted in figure 2 and compared with the logarithmic velocity profile in turbulent flow over a smooth plate:

$$U^+ = \frac{U(z)}{u_*} = \frac{1}{\kappa}\ln(z^+) + B, \tag{3.1}$$

where $B = 5.1$, and the wall unit ν/u_* serves as the length scale; ν is the kinematic viscosity of air; the scaled variables are denoted by '+'. The values of U_{10}, estimated by extrapolating (1.1) to $z = 10$ m, vary with fetch by less than 6 %; the mean values of U_{10} are specified in table 1.

The slopes of the velocity profiles in the logarithmic innermost part of the boundary layers (Zavadsky & Shemer 2012) are very close to that of the smooth solid surface. It is evident that at each fetch, the profiles are shifted down with an increase in wind velocity. A similar downshift of profiles with u_* was observed in the detailed PIV measurements performed by Buckley *et al.* (2020) at a significantly larger fetch ($x = 22.7$ m). For a given friction velocity u_*, the downshift of profiles with fetch is observed in this figure. This finding indicates that for young wind waves, the value of the Charnock constant in (1.2) varies with x. It thus seems appropriate to apply an alternative to the (1.1) approach to describe the shape of the turbulent velocity profiles over wind waves that is based on the directly measured quantities.

The vertical shift in the velocity profiles, as presented in figure 2, was treated for solid rough surface by Clauser (1954) and Hama (1954) who modified the smooth velocity

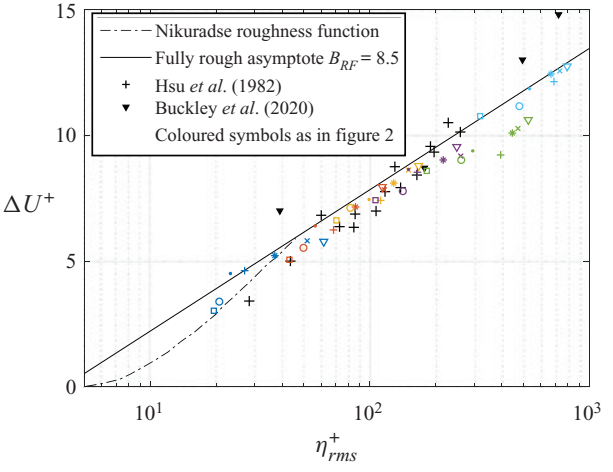

Figure 3. Hama roughness function $\Delta U^+(\overline{\eta^2}^{1/2}u_*/\nu)$. Colours and markers as in figure 2.

profile (3.1) to

$$U^+(z^+) = \frac{1}{\kappa}\ln(z^+) + B - \Delta U^+, \tag{3.2}$$

where the amount of the downshift ΔU^+ depends on the dimensionless characteristic roughness height k_s^+. Hudson, Dykhno & Hanratty (1996) measured the statistical characteristics of the turbulent boundary layer over a solid wavy surface and suggested using the wave height as the appropriate vertical roughness scale. Inspired by this approach, the local dimensionless surface roughness of random wind waves that evolve with fetch is parametrized here by the local characteristic r.m.s. values of the surface elevation $k_s^+ = \eta^+_{rms} = (\overline{\eta(x)^2})^{1/2}u_*/\nu$. It should be stressed that drift current at the water surface induced mainly by wind shear exists and is estimated as $0.2u_* < u_s < 0.5u_*$ (Toba 1988; Tseng *et al.* 1992; Caulliez *et al.* 2008; Zavadsky & Shemer 2017*b*). This drift, however, does not affect the outcome notably because ΔU^+ represents the difference in velocities over the smooth and wave water surfaces, so that the contribution of u_s is cancelled.

The validity of this parametrization is examined in figure 3 where the dimensionless downshift ΔU^+ is plotted as a function of the local η^+_{rms}. The coloured markers denote the dimensionless downshift ΔU^+ estimated from the velocity profiles, see figure 2, the black symbols represent estimates of ΔU^+ made on the basis of the alternative published data.The broken line corresponds to the roughness functions $\Delta U^+(\eta^+_{rms})$ given by

$$\Delta U^+ = \frac{1}{\kappa}\ln(\eta^+_{rms}) + B - B_{RF}, \tag{3.3}$$

with B_{RF} defined by Nikuradse (1950). The roughness function ΔU^+ in the fully rough regime corresponds to $B_{RF} = 8.5$ and is plotted by a solid line.

Nikuradse estimated that for monodisperse close-packed sand grain roughness, the onset of the fully rough regime occurs at $k_s^+ \approx 70$. However, the roughness type and uniformity may advance the onset of a fully rough boundary layer, see Schultz & Flack (2007) and references therein. As documented by Liberzon & Shemer (2011), Zavadsky & Shemer (2017*a*) and Shemer *et al.* (2020), the characteristic water surface roughness η_{rms} increases

with the fetch x for a constant friction velocity u_*, and with u_* for a constant fetch. Figure 3 demonstrates that the downward shift ΔU^+ increases with the scaled surface roughness η^+_{rms} and follows the expected fully rough asymptote for majority of cases examined here.

The results obtained at diverse wind velocities and fetches in three different facilities thus correspond fairly well to fully rough conditions with η_{rms} serving as the characteristic roughness. Therefore, the fully rough velocity profile over wind-generated waves at each fetch x in all those cases can be presented as

$$U^+(x, z) = \frac{1}{\kappa} \ln\left(\frac{z}{\eta_{rms}(x)}\right) + 8.5. \tag{3.4}$$

It is evident from (3.4) that the shapes of the mean velocity profile in the overlap region are unaffected by the roughness η_{rms}, which determines only their vertical shift. This wall similarity directly relates the shape of the velocity profile to the local characteristic wave height.

Comparison of (3.4) and (1.1) allows for relating the roughness parameter z_0 to the directly measurable characteristic surface elevation variation, yielding for a fully rough surface $\eta_{rms} \approx 30 z_0$ that can be measured relatively easily. It is thus preferable to use (3.4) to characterize the shape of the velocity profile in air over wind waves. In particular, (3.4) enables determination of the commonly adopted characteristic wind velocity estimated at $z = 10$ m over the water surface, U_{10}.

Additional insight into interaction of wind and waves may be gained by analysing the integral boundary layer parameters based on the measured velocity profiles. The variation of the estimated values of the boundary layer thickness δ, the displacement thickness $\delta_1 = \int_0^\delta (1 - U(z)/U_0)\,\mathrm{d}z$ and the momentum thickness $\delta_2 = \int_0^\delta (U(z)/U_0)(1 - U(z)/U_0)\,\mathrm{d}z$ with fetch x are plotted in figure 4(*a–c*) for the wind velocities given in table 1. Note that to calculate δ_1 and δ_2, the lower part of the velocity profile adjacent to the interface was approximated using the lin-log velocity profile suggested by Miles (1957) that smoothly connects the linear viscous sublayer to the logarithmic overlap region.

Jimenez (2004) asserted that wall similarity holds once the roughness height k is sufficiently small, so that $\delta/k > 40$. The relative height of the roughness manifested by the ratio of the boundary layer thickness and the characteristic wave amplitude δ/a, where $a = \sqrt{2}\eta_{rms}$, decreases with wind velocity, see figure 4(*d*). The values of δ/a are below the limit of Jimenez (2004). Nevertheless, as demonstrated in figure 3, wall similarity is maintained in all those cases. This finding supports the applicability of a lower critical value of $\delta/k = 5$ suggested by Castro (2007).

The dimensionless velocity defect values $U_0^+ - U^+$ measured in our facility at multiple fetches and wind velocities presented in figure 2 are plotted in figure 4(*e*). The values of u_* given in table 1 are used for normalization. It is evident that in this representation, all velocity profiles collapse. The roughness effects that may destruct the near-wall coherent structures are thus confined to the inner layer, i.e. the innermost part of the boundary layer. This feature of the velocity profiles implies wall similarity (Raupach, Antonia & Rajagopalan 1991). The distributions of the normalized Reynolds shear stress $-\overline{u'w'}^+$ plotted for those conditions in figure 4(*f*) also collapse. The scatter in figure 4(*e–f*) may be attributed to variations of the friction velocity u_* with fetch that are estimated at approximately 7 %. Figure 4(*e–f*) thus provide additional evidence for the existence of wall similarity of the overlap and outer layers over young wind waves.

The airflow in the test section is maintained by a favourable pressure gradient. Boundary layer similarity in the presence of the pressure gradient requires that the Clauser parameter

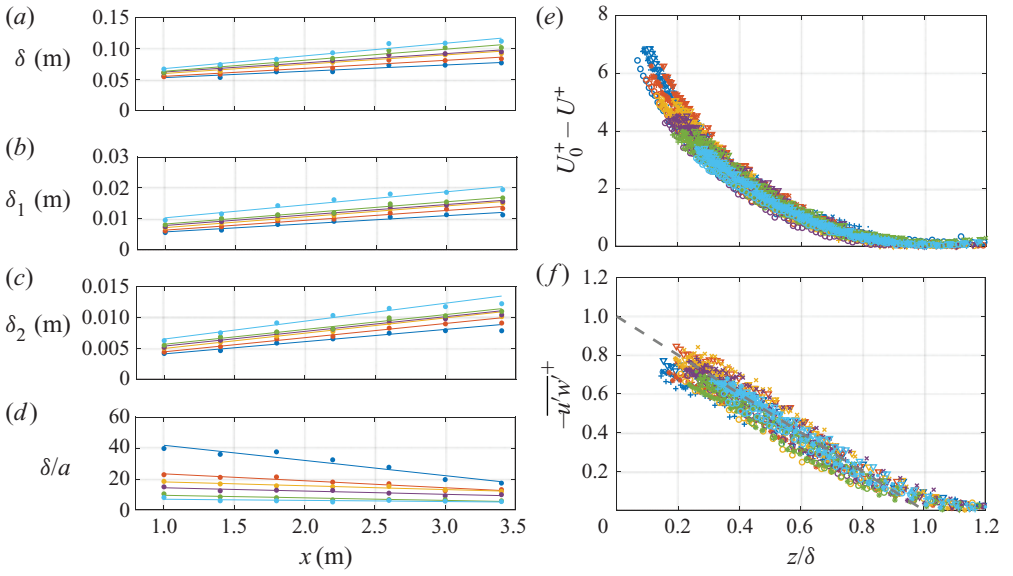

Figure 4. Boundary layer characteristics: (*a*) boundary layer thickness; (*b*) displacement thickness; (*c*) momentum thickness; (*d*) ratio of boundary thickness and roughness height $a = \sqrt{2}\eta_{rms}$; (*e*) vertical profile of normalized Reynolds stress; (*f*) velocity defect profiles using mixed outer scale at all conditions in figure 2. Colours in panels (*a–d*) and symbols in panels (*e*,*f*) as in figure 2.

remains constant (White 2006):

$$\beta = \frac{\delta_1}{\tau}\frac{\mathrm{d}p}{\mathrm{d}x}. \tag{3.5}$$

The values of β evaluated for the present experimental conditions based on direct pressure drop measurements presented in Liberzon & Shemer (2011), and on the displacement thickness presented in figure 4(*b*), yield β that do not change significantly and remain in the range from -0.17 to -0.1. Note that the slope of the dimensionless Reynolds stress with the dimensionless vertical coordinate, presented by a dashed line in figure 4(*f*), equals to -1, allowing independent evaluation of the Clauser parameter as

$$\beta = -\frac{\delta_1}{\delta}\frac{\partial(\overline{u'w'}^{+})}{\partial(z/\delta)} \approx -\frac{\delta_1}{\delta} \tag{3.6}$$

that is consistent with (3.5), see figure 4(*a*,*b*). To further support the equilibrium boundary layer defined by Clauser, the values of the defect shape factor, defined as

$$G = \frac{u_*}{\delta_1 U_0}\int_0^{\delta}\left(\frac{U_0 - U(z)}{u_*}\right)^2 \mathrm{d}z, \tag{3.7}$$

were calculated and are presented in table 2. Nearly constant values of G in this table provide further support for invariance of the velocity defect profile (Mellor & Gibson 1966).

4. Drag coefficients over wind waves

The friction at the water surface is commonly quantified in wind wave modelling and meteorology studies using U_{10} that serves as the velocity scale. Following Donelan (1998) and Donelan *et al.* (2004), the corresponding drag coefficient is defined

x (m)	—	1	1.4	1.8	2.2	2.4	3.0	3.4
	5.5	4.77	5.07	5.32	5.49	5.58	5.76	5.75
	6.6	4.95	5.12	5.37	5.39	5.43	5.66	5.70
U_0 (m s^{-1})	7.7	4.97	5.15	5.17	5.25	5.34	5.55	5.62
	8.9	4.79	4.93	5.04	5.03	5.05	5.11	5.25
	10.05	4.65	4.81	4.76	4.71	4.89	4.96	5.08
	11.2	4.56	4.68	4.76	4.82	4.81	4.85	4.91

Table 2. Values of defect shape factor G computed by (3.7) for all fetches and wind forcing. The r.m.s. of the data is 5.13 with a standard deviation of 0.33.

as $C_D = (u_*/U_{10})^2$. The results of Donelan *et al.* (2004) plotted in figure 5(*a*) agree reasonably well with those derived from the laboratory measurements (Mitsuyasu 1970; Mitsuyasu & Honda 1974, 1982; Caulliez *et al.* 2008; Buckley *et al.* 2020) and the values of C_D derived from the data presented in table 1. The field results of Mitsuyasu (1969) are included in this figure as well. The plotted values of C_D were estimated using the values of u_* and U_{10} reported in those references.

Note that the results of Donelan *et al.* (2004) indicate that the saturation of C_D is attained at wind velocities U_{10} exceeding approximately 40 m s^{-1}. Wu (1969) observed similar saturation at $U_{10} > 15$ m s^{-1}; he attributed it to the fact that at those conditions, the water surface becomes fully rough with k_s^+ based on the Nikuradze sand grain height exceeding 70. The present results, however, demonstrate that the velocity downward shift follows the fully rough asymptote even at notably lower wind velocities. Thus, the water surface may become effectively fully rough, while the friction coefficient C_D is still well below its saturation level.

The effect of the surface roughness, manifested in the vertical displacement of similar velocity profiles as compared to the smooth-wall case, results in a momentum deficit related to the momentum exchange between airflow and waves. The skin-friction factor, defined as $c_f = 2(u_*/U_0)^2$, is related to the momentum deficit. The integral momentum equation in the presence of pressure gradient applied in Appendix B to relate c_f to x/k_s. Figure 6 in this appendix demonstrates that for the Clauser parameters encountered in the present study, the resulting relation does not differ notably from that obtained for a fully rough turbulent boundary layer over a surface with a constant roughness k_s in the absence of a pressure gradient (Prandtl & Schlichting 1934; Schlichting 1979) :

$$c_f = [2.87 + 1.58 \log_{10}(x/k_s)]^{-2.5}. \tag{4.1}$$

The skin friction is the governing parameter that couples the airflow with water waves and shear current. The values of c_f evaluated using (4.1) that relate the data on airflow and water-wave measurements acquired in various studies are presented in figure 5(*b*). To compare results of multiple studies on wind waves, the dimensionless customary adopted fetch $\hat{x} = xg/u_*^2$ is used. All studies show that the increase in $\hat{x}$ results in a decrease of c_f. In the inset to figure 5(*b*), the values of c_f from (4.1) are compared with $2(u_*/U_0)^2$ showing reasonable agreement. Note that although constant roughness is assumed in derivation of (4.1), the fetch-dependent effective roughness $\eta_{rms}(x)$ is used. The applicability of (4.1) supports the conjecture that the turbulent boundary layer in airflow over young water waves indeed satisfies wall similarity over a rough wavy water surface. The inset indicates that for

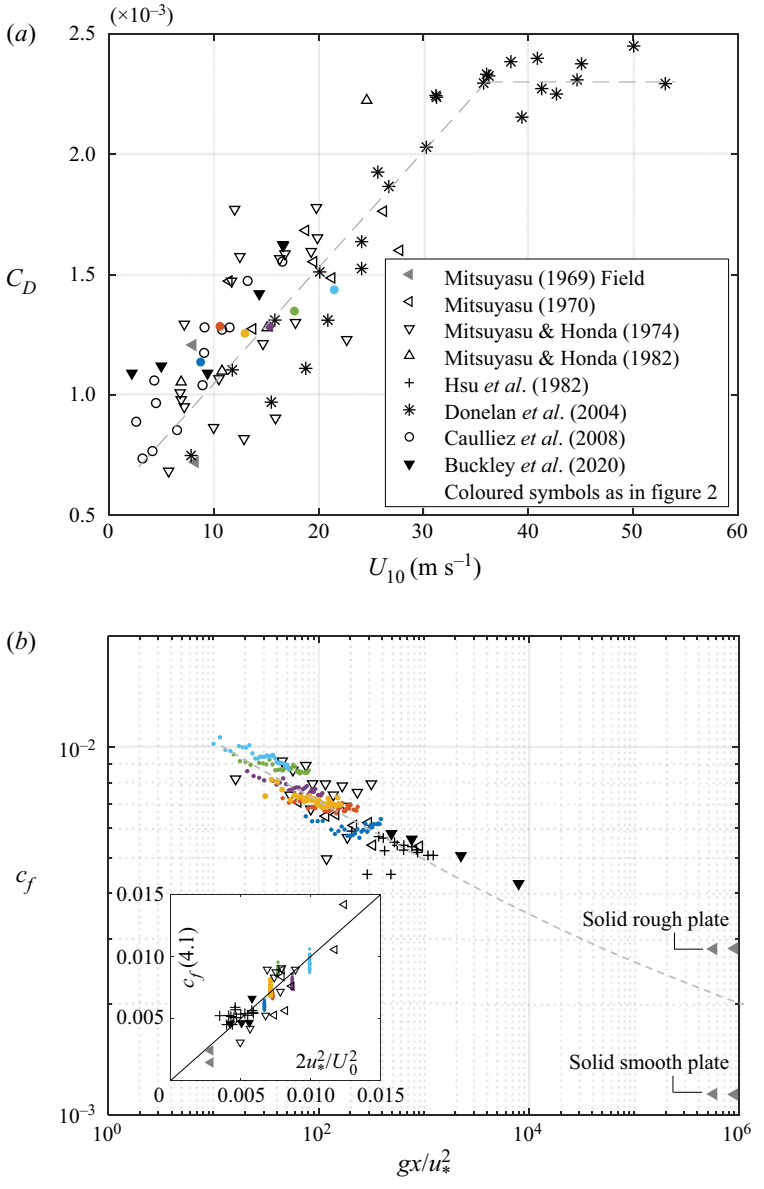

Figure 5. Drag coefficients: (*a*) $C_D = (u_*/U_{10})^2$; (*b*) local friction factor c_f. Marker values according to (4.1) with $k_s = \eta_{rms}$. Inset shows c_f obtained by (4.1) versus $2(u_*/U_0)^2$.

each U_0, the values of c_f practically do not depend on the fetch, as observed in fully rough flows over a solid surface with $k_s \sim x$. As demonstrated in Appendix B, in the present experiments, the characteristic amplitude of the young wind waves η_{rms} in fact increases approximately linearly with x for each wind velocity U_0.

While the majority of the available results were obtained in laboratory facilities, results of field measurements reported by Mitsuyasu (1969) were also included in figure 5(*b*) and allowed to extend the range of dimensionless fetches $\hat{x}$ to six orders of magnitude. The fully rough estimates are based on the reported values of the fetch x and η_{rms}, while the

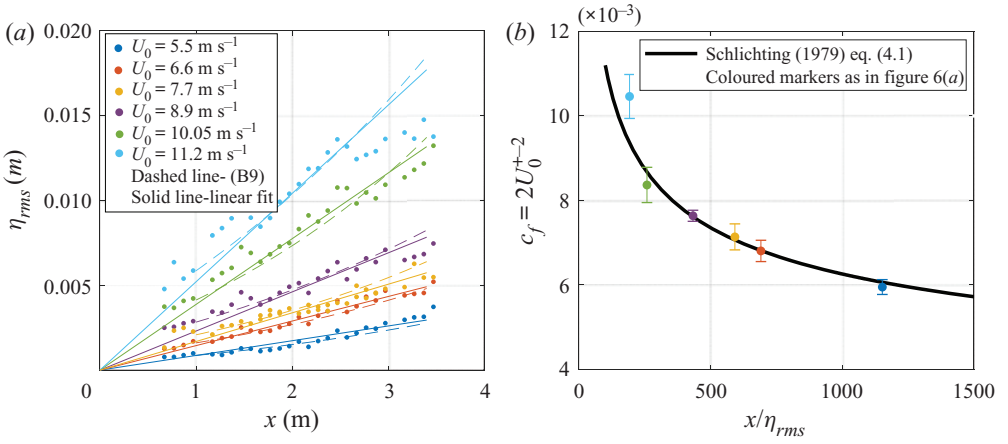

Figure 6. (*a*) Surface elevation as a function of x for various wind velocities: solid lines, linear fits; dashed lines, numerical solution of (B9). (*b*) Skin-friction coefficient dependence on dimensional fetch; solid line corresponding to (4.1) for rough flow with no pressure gradient is plotted for comparison. Coloured markers, the mean values of c_f presented in table 1 as a function of the values of x/η_{rms} estimated from figure 6(*a*).

smooth surface values correspond to the flow over a flat plate at high Reynolds numbers (Schlichting 1979). It should be stressed that the wave steepness in laboratory experiments is usually significantly higher than that in field studies. The characteristic wave steepness measured directly by Zavadsky & Shemer (2017*a*) using a laser slope gauge does not vary significantly with fetch, in spite of wave amplitude growth. For all wind velocities applied in their experiments, the measured values of the characteristic steepness remain close to $\epsilon = 0.2$. Similar values of the measured steepness were reported by Hsu *et al.* (1982) and Buckley *et al.* (2020). Buckley *et al.* (2020) demonstrated that at those values of ϵ, the total skin friction is mostly determined by the form drag, whereas the contribution of the viscous drag is relatively minor. This observation is consistent with the statement by Flack & Schultz (2014) that a fully rough regime is characterized by the dominant contribution of the form drag of the roughness elements. Moreover, according to Buckley *et al.* (2020), for $\epsilon \approx 0.2$, the entire wind stress is transferred to the wave motion, whereas at $\epsilon < 0.1$, less than 50 % is transmitted. In the field experiments of Mitsuyasu (1969), the estimated wave steepness is $\epsilon \approx 0.05$. It can be seen from figure 5(*b*) that both rough and smooth surface estimates of c_f yield results of the same order of magnitude. Note that extrapolation of the experimentally estimated values of c_f to higher dimensionless fetches, attempted by a broken line in figure 5(*b*), suggests that the friction factors may fall within these extreme values. Although the wave ages c_p/u_* for the flow conditions in figure 2 do not exceed unity, the results presented in figure 5(*b*) may be applicable also for faster moving longer waves.

5. Discussion and conclusions

Coupling between airflow and water waves is studied here on the basis of extensive experimental data on velocity profiles in air over wind waves at different wind velocities and fetches accumulated in our wind wave tank. The wind velocity information is associated with the corresponding data on the characteristic parameters of wind waves. When possible, analysis is supported by data extracted from additional laboratory studies, as well as from reports on field measurements. We also take advantage of the considerable

progress made in recent decades in the analysis of turbulent flows over solid rough surfaces where the wall similarity of turbulent boundary layer has been studied in detail for a variety of geometric parameters. We apply this approach to air flow over the perpetually moving wavy water surface.

The moving three-dimensional random water surface is characterized by a wide spectrum of wavelengths that may evolve in time as well as in space. It is thus considerably more complicated than the 'frozen' rough solid surface that, in most studies, is assumed as spatially homogeneous. The airflow over wind waves differs from that over a solid surface in several important aspects. The dynamic coupling between the airflow and wind waves results in a transfer of energy and momentum from wind to the water surface causing wind wave growth; this effect does not exist in the case of a rigid surface. In measurements of a solid rough surface, the vertical distance from the surface at the sensor location remains fixed, whereas in water wave experiments, the elevation of the sensor over the instantaneous surface level varies continuously. Special effort was therefore invested by Zavadsky & Shemer (2012) in the determination of the mean surface elevation at each fetch and wind forcing conditions that may be different from the still surface level; the mean wind velocity profiles were obtained relative to this reference height. The movement of the interface becomes even more essential in the determination of the turbulent parameters of the airflow above the water surface. There seems to be no straightforward way to decouple the velocity fluctuations that are intrinsic to the turbulent airflow, from variations related to the random water surface movement. First, as mentioned above, the elevation of the sensor relative to the instantaneous local surface position varies in time and may cause fluctuations in the measured velocity. Second, the wavy motion observed in water also exists in air. The corresponding airflow orbital velocities have a wide spectrum related to the spectrum of the surface elevation in the presence of wind waves; the phases of those fluctuations are random. The fluctuations associated with waves in airflow decay exponentially with height above the mean surface. These two phenomena result in the characteristic fluctuations of the horizontal, $\overline{u'^2}^{1/2}$, and vertical, $\overline{w'^2}^{1/2}$, velocity components, that at low elevations are notably higher than the corresponding values measured in boundary layers over smooth and rough surfaces (Zavadsky & Shemer 2012). An additional but less important complication is related to the drift current induced by wind shear as well as by the water waves' nonlinearity.

Probably for those reasons, the structure of the turbulent boundary layer over wind waves so far has not been related directly to their characteristics. The roughness parameter z_0 that was introduced empirically to describe the wind velocity profile over waves cannot be easily related to water surface properties. We suggest using the measurable characteristic wave amplitude η_{rms} as an analogue to the roughness k_s that characterizes flows over rough surfaces. Laboratory-scale experiments necessarily study the so-called 'young' wind waves characterized by wave steepness that often exceeds that commonly encountered in the open sea. The water surface in the presence of young wind waves is thus effectively fully rough. Although under steady wind forcing the wave height increases with fetch, the characteristic steepness remains essentially unchanged along the test section. In this sense, the water surface in a wind wave tank retains approximately similar geometry. Note that experiments show that the friction velocity u_* also does not vary significantly with x for a constant wind velocity U_0.

In the current study, we have demonstrated the existence of wall similarity in the spatially developing boundary layer over wind waves. The invariance of the velocity-defect profiles in figure 4(e,f) implies that the direct influence of the local water surface

roughness $k_s = \eta_{rms}(x)$ is confined to the inner part of the boundary layer. The downward shift of the velocity profiles ΔU^+ corresponds to the rise in momentum deficit that is directly related to increase in frictional drag. It was found that when the roughness is taken as $k_s = \eta_{rms}$, ΔU^+ follows the fully rough asymptote. This implies that for young wind wave studies, the wall shear stress is almost entirely owing to form drag, in agreement with Buckley *et al.* (2020). It should be stressed that the onset of a fully rough regime in flow over wind waves occurs at roughness η^+_{rms} that is considerably below Nikuradse's criterion $k_s^+ > 70$. This may be attributed to a difference in the roughness type. Under all experimental conditions in our facility, wall similarity was found up to $\delta/a \approx 5$, where the characteristic wave amplitude is defined as $a = \sqrt{2}\eta_{rms}$, in agreement with the limit over a solid surface found by Castro (2007).

The coupling between airflow and water surface is characterized by the drag coefficients. The values of C_D in our experiments agree well with data available elsewhere, see figure 5(*a*). Definition of C_D based on a wind velocity characterized by U_{10} is physically irrelevant in a laboratory facility; it is thus more sensible to use the maximum wind velocity U_0 that defines the skin-friction coefficient $c_f = 2(u_*/U_0)^2$ that is related to the derivative of the momentum thickness, (A2). Fully rough flows over solid surfaces are dominated by pressure drag, the momentum integral combined with the rough wall-velocity profile leads to a relation $c_f = f(x/k_s)$ that agrees well with (4.1), see Appendix B. For fully rough conditions in our wind wave experiments, this relation is applicable under various wind velocities and agrees with the constant with an x estimate of $2(u_*/U_0)^2$, figure 5(*b*). Similar to fully rough regime over solid surfaces, constant c_f in a developing boundary layer is possible only when x/k_s remains constant (Chung *et al.* 2021). This occurs when the vertical and horizontal scales of the roughness grow linearly along the plate (Talluru *et al.* 2016; Sridhar, Pullin & Cheng 2017). We have shown that c_f obtained at the interface of the wavy water surface depends entirely on $x/\eta_{rms}(x)$ and indeed does not vary notably. To the best of our knowledge, this finding has not yet been reported in boundary layers over wind waves. Because c_f depends merely on the local surface elevation, the shear stress responsible for the momentum flux into the wave field can be evaluated as well.

Funding. This study was supported by grant 508/19 from Israel Science Foundation. Partial support to M.G. by Ben Gurion University is gratefully acknowledged.

Declaration of interests. The authors report no conflict of interest.

Author ORCIDs.
Meital Geva https://orcid.org/0000-0002-8035-1905;
Lev Shemer https://orcid.org/0000-0003-0158-1823.

Appendix A. An evaluation of the friction velocity using momentum integral equation

Friction velocities can be estimated independently using the momentum integral equation that, in the presence of a pressure gradient, can be written as

$$\frac{u_*^2}{U_0^2} = \frac{\mathrm{d}\delta_2}{\mathrm{d}x} - (2\delta_2 + \delta_1)\frac{1}{\rho U_0^2}\frac{\mathrm{d}p}{\mathrm{d}x}. \tag{A1}$$

Here δ, δ_1 and δ_2 are the boundary layer thickness, the displacement thickness and the momentum thickness, respectively. Because $-\partial(\overline{u'w'}^+)/\partial(z/\delta) \approx -1$ (figure 4*f*),

x (m)	—	1.4	1.8	2.2	2.4	3.0	3.4
	5.5	0.28	0.29	0.30	0.30	0.30	0.31
	6.6	0.37	0.38	0.39	0.39	0.39	0.40
U_0 (m s^{-1})	7.7	0.45	0.47	0.47	0.47	0.48	0.49
	8.9	0.51	0.53	0.54	0.54	0.54	0.55
	10.05	0.59	0.60	0.61	0.60	0.61	0.61
	11.2	0.74	0.76	0.78	0.78	0.77	0.77

Table 3. Values of friction velocity in m s^{-1} computed by (A3) for data in figure 4(a–c).

substituting (3.5) and (3.6) into (A1) results in

$$\frac{u_*^2}{U_0^2} \approx \frac{\mathrm{d}\delta_2}{\mathrm{d}x} + \frac{(2\delta_2 + \delta_1)}{\delta}\frac{u_*^2}{U_0^2}. \tag{A2}$$

Rearranging (A2) yields a simple approximation for u_*,

$$u_* = U_0\sqrt{\frac{\mathrm{d}\delta_2}{\mathrm{d}x} \Big/ \left(1 - \frac{2\delta_2 + \delta_1}{\delta}\right)}. \tag{A3}$$

Estimates of δ, δ_1 and δ_2 presented in figure 4(a–c) allow therefore to obtain the values of u_* for all wind forcing conditions at six fetches; the results are listed in table 3.

Table 3 shows that for the given wind velocity U_0, the values of u_* remain nearly constant along the test section, in agreement with the available laboratory studies (Mitsuyasu & Rikiishi 1978; Hsu *et al.* 1982; Caulliez *et al.* 2008; Zavadsky & Shemer 2012). For lower wind velocities, $U_0 \leqslant 8.9$ m s^{-1}, the average values of u_* agree well with the friction velocities in table 1. For the two higher wind velocities, estimates based on the momentum integral yield values approximately 10 % smaller than those derived from the velocity profile fit, see table 1. Owing to inherent difficulties in the measurements of airflow close to the interface in the presence of large random wind waves under those wind forcing conditions, for $U_0 = 10.05$ and 11.2m s^{-1}, Zavadsky & Shemer (2012) extended the fitting domain up to $z/\delta < 0.3$ instead of $z/\delta < 0.2$ applied for lower wind velocities. This extension to the outer part of the boundary layer apparently caused incorporation in the fitting domain of a small portion of the wake region, which resulted in overestimate of the friction velocities. Nevertheless, application of the integral momentum method, which is less sensitive to the inner region, shows that the resulting error is relatively small and comparable with the experimental uncertainty. The average value of u_* was computed for each wind velocity U_0; the corresponding averages denoted as $u_{*,MI}$ are listed in table 1. All values of u_* presented in table 1 agree well with Plant & Wright (1977). The use of the momentum integral (A1) thus provides reasonably accurate prediction of the friction velocity in air flow over young wind waves at all wind forcing conditions.

Appendix B. Estimates of $c_f = f(x/k_s, \Pi)$ based on the momentum integral equation

The integral momentum equation approach applied by Prandtl & Schlichting (1934) and Schlichting (1979) to derive the skin-friction coefficient dependence on fetch $c_f = f(x/k_s)$ for airflow above a fully rough surface is extended here to account for the presence of a

pressure gradient and the fetch dependence of roughness k_s. The velocity profile in the overlap and in the outer layers of fully rough flows can be presented as

$$U^+(z) = \frac{1}{\kappa}\ln\left(\frac{z}{k_s}\right) + B_{RF} + \frac{2\Pi}{\kappa}\sin^2\left(\frac{\pi z}{2\delta}\right). \tag{B1}$$

Here $B_{RF} = 8.5$ and Π is the Cole's wake parameter that depends on the Clauser's pressure parameter β only (White 2006). At the edge of the boundary layer $z = \delta$,

$$U_0^+ = \sqrt{\frac{2}{c_f}} = \frac{1}{\kappa}\ln\left(\frac{\delta}{k_s}\right) + B_{RF} + \frac{2\Pi}{\kappa}. \tag{B2}$$

The ratio of the boundary layer thickness and the equivalent sand grain roughness is thus

$$\frac{\delta}{k_s} = \exp\left(\kappa\left(U_0^+ - B_{RF} - \frac{2\Pi}{\kappa}\right)\right). \tag{B3}$$

The displacement thickness δ_1 and the momentum thickness δ_2 for the velocity profile given by (B1) are (Sridhar *et al.* 2017)

$$\delta_1 = \delta\frac{1+\Pi}{\kappa B_{RF} + 2\Pi + \ln\dfrac{\delta}{k_s}}, \tag{B4a}$$

$$\delta_2 = \delta\frac{\Pi^2 - 4 + 2\kappa B_{RF}(1+\Pi) + 2(1+\Pi)\ln\dfrac{\delta}{k_s} - 4\Pi Q/\pi}{2\left(\kappa B_{RF} + 2\Pi + \ln\dfrac{\delta}{k_s}\right)^2}. \tag{B4b}$$

Here, $Q = \int_0^\pi \sin(z)/z\,\mathrm{d}z = 1.85$. It follows from (B2) and (B4) that

$$\delta_1 = \delta\frac{1+\Pi}{\kappa U_0^+}, \tag{B5a}$$

$$\delta_2 = \delta\left[\frac{\Pi^2 - 4 - 4\Pi(1+\Pi) - 4\Pi Q/\pi}{2\left(\kappa U_0^+\right)^2} + \frac{1+\Pi}{\kappa U_0^+}\right] = \delta G(U_0^+, \Pi). \tag{B5b}$$

Because δ_1/δ and δ_2/δ depend on U_0^+ and Π, (A2) can be rearranged as

$$\frac{\mathrm{d}\delta_2}{\mathrm{d}x} = \frac{1}{U_0^+}\left(1 - \frac{2\delta_2 + \delta_1}{\delta}\right) = F(U_0^+, \Pi) \tag{B6}$$

so that (B6) and (B5*b*) yields

$$\frac{\mathrm{d}\delta_2}{\mathrm{d}x} = G\frac{\mathrm{d}\delta}{\mathrm{d}x} + \delta\frac{\partial G}{\partial U_0^+}\frac{\mathrm{d}U_0^+}{\mathrm{d}x} + \delta\frac{\partial G}{\partial \Pi}\frac{\mathrm{d}\Pi}{\mathrm{d}x} = F. \tag{B7}$$

In the present study, this relation is simplified because $\mathrm{d}U_0^+/\mathrm{d}x = 0$,

$$\frac{\mathrm{d}\delta}{\mathrm{d}x} = \frac{F - \delta\dfrac{\partial G}{\partial \Pi}\dfrac{\mathrm{d}\Pi}{\mathrm{d}x}}{G}. \tag{B8}$$

U_0 (m s^{-1})	$\alpha^{-1} = x/\eta_{rms}$	$c_{f,ZS}$	$c_{f,MI}$
5.5	1152.3	0.0056	0.0060
6.6	691.0	0.0063	0.0070
7.7	592.0	0.0068	0.0075
8.9	433.7	0.0079	0.0074
10.05	258.1	0.0092	0.0074
11.2	192.0	0.0115	0.0095

Table 4. Experimental values of x/η_{rms} obtained as inverse of slopes in figure 6(a) and skin friction coefficients using u_* values specified in table 1. Here, subscript ZS refers to Zavadsky & Shemer (2012) and MI refers to the momentum integral equation.

For a given $\Pi(x)$ and U_0^+, this relation can be solved by a numerical integration procedure resulting in $\delta = \Phi(x)$ leading to a relation for $k_s(x)$ based on (B3),

$$k_s = \frac{\Phi(x)}{\exp(\kappa(U_0^+ - B_{RF} - 2\Pi(x)/\kappa))}. \tag{B9}$$

Fitting the velocity distributions in figure 2 to (B1) leads to the Coles' parameter estimates as $\Pi \approx 0.1x$. This dependence was substituted in (B8) and for a given U_0^+, this equation was integrated by a fourth-order Runge–Kutta integration routine with initial value of $\delta \approx 0.05$ m at $x = 1$ m. The variations of k_s with downstream distance x were computed using (B9) and plotted in figure 6(a) by dashed lines; the experimental results are plotted in this figure as well. Linear fits were also added to the scatter at each wind forcing (solid lines). At each wind velocity U_0, the results exhibit a reasonably accurate linear fit, with the scatter that increases somewhat for the highest wind velocity. Talluru *et al.* (2016) and Sridhar *et al.* (2017) showed that in boundary layers over a rough solid surface, c_f remains constant when the roughness varies linearly with x. This condition is satisfied reasonably well for the present experiments. The approximately linear with x growth of the water surface roughness represented by η_{rms} enables estimation of the values of $x/\eta_{rms} = x/k_s$ based on the fit slopes (table 4). The values of $c_f = 2u_*^2/U_0^2$ in this table are evaluated using the friction velocities listed in table 1 and were plotted versus x/η_{rms} with the corresponding error bars (figure 6b). The solid line corresponds to the case of the turbulent flow over a surface with a constant roughness in the absence of a pressure gradient (4.1) and agrees fairly well with the present results. The curve in figure 6(b) allows for a reasonably accurate estimate of the characteristic surface elevation for young wind waves in any fetch for a given u_*/U_0. It should be stressed that the effect of a small favourable pressure in the present experiments ($\beta < 0.2$) is practically negligible.

References

Buckley, M.P., Veron, F. & Yousefi, K. 2020 Surface viscous stress over wind-driven waves with intermittent airflow separation. *J. Fluid Mech.* **905**, A31.

Bye, J.A.T, Ghantous, M. & Wolff, J.O. 2010 On the variability of the charnock constant and the functional dependence of the drag coefficient on wind speed. *Ocean Dyn.* **60** (4), 851–860.

Bye, J.A.T & Wolff, J.O. 2008 Charnock dynamics: a model for the velocity structure in the wave boundary layer of the air–sea interface. *Ocean Dyn.* **58** (1), 31–42.

Castro, I.P. 2007 Rough-wall boundary layers: mean flow universality. *J. Fluid Mech.* **585**, 469–485.

Caulliez, G., Makin, V. & Kudryavtsev, V. 2008 Drag of the water surface at very short fetches: observations and modeling. *J. Phys. Oceanogr.* **38** (9), 2038–2055.

CHARNOCK, H. 1955 Wind stress on water surface. *Q. J. R. Meteorol. Soc.* **81**, 639–640.
CHUNG, D., HUTCHINS, N., SCHULTZ, M.P. & FLACK, K.A. 2021 Predicting the drag of rough surfaces. *Annu. Rev. Fluid Mech.* **53**, 439–471.
CLAUSER, F.H. 1954 Turbulent boundary layers in adverse pressure gradients. *J. Aerosol Sci.* **21**, 91–108.
CSANADY, G.T. 2001 *Air-Sea Interaction*. Cambridge University Press.
DONELAN, M.A. 1998 Air-water exchange processes. In *Physical Processes in Lakes and Oceans* (ed. J. Imberger), vol. 54, pp. 19–36. Coastal and Estuarine Studies.
DONELAN, M.A., DOBSON, F.W., SMITH, S.D. & ANDERSON, R.J. 1993 On the dependence of sea surface roughness on wave development. *J. Phys. Oceanogr.* **23** (9), 2143–2149.
DONELAN, M.A., HAUS, B.K., REUL, N., PLANT, W.J., STIASSNIE, M., GRABER, H.C., BROWN, O.B. & SALTZMAN, E.S. 2004 On the limiting aerodynamic roughness of the ocean in very strong winds. *Geophys. Res. Lett.* **31**, L18306.
DRENNAN, W.M., TAYLOR, P.K. & YELLAND, M.J. 2005 Parameterizing the sea surface roughness. *J. Phys. Oceanogr.* **35**, 835–848.
FLACK, K.A. & SCHULTZ, M.P. 2014 Roughness effects on wall-bounded turbulent flows. *Phys. Fluids* **104**, 101305.
FLACK, K.A., SCHULTZ, M.P. & BARROS, J.M. 2020 Skin friction measurements of systematically-varied roughness: probing the role of roughness amplitude and skewness. *Flow Turbul. Combust.* **104**, 317–329.
HAMA, F.R. 1954 Boundary-layer characteristics for rough and smooth surfaces. *Trans. Soc. Nav. Archit. Mar. Engrs* **62**, 333–351.
HRISTOV, T.S., MILLER, S.D. & FRIEHE, C.A. 2003 Dynamical coupling of wind and ocean waves through wave-induced air flow. *Nature* **422** (6927), 55–58.
HSU, C.T, WU, H.Y., HSU, E.Y. & STREET, R.L. 1982 Momentum and energy transfer in wind generation of waves. *J. Phys. Oceanogr.* **12** (9), 929–951.
HUDSON, J.D., DYKHNO, L. & HANRATTY, T.J. 1996 Turbulence production in flow over a wavy wall. *Exp. Fluids* **20**, 257–265.
JANSSEN, P.A.E.M. 1989 Wave-induced stress and the drag of air flow over sea waves. *J. Phys. Oceanogr.* **19** (6), 745–754.
JANSSEN, P.A.E.M. 2008 Air-sea interaction through waves. In *ECMWF Workshop on Ocean-Atmosphere Interactions*, pp. 47–60.
JIMENEZ, J. 2004 Turbulent flows over rough walls. *Annu. Rev. Fluid Mech.* **36**, 173–196.
KAWAMURA, H., OKUDA, K., SANSHIRO, K. & YOSHIKAI, T. 1981 Structure of turbulent boundary layer over wind waves in a wind wave tunnel. *Tôhoku Geophys. J.* **28** (2), 69–86.
KAWAMURA, H. & TOBA, Y. 1988 Ordered motion in the turbulent boundary layer over wind waves. *J. Fluid Mech.* **197**, 105–138.
LI, S., ZOU, Z., ZHAO, D. & HOU, Y. 2020 On the wave state dependence of the sea surface roughness at moderate wind speeds under mixed wave conditions. *J. Phys. Oceanogr.* **50** (11), 3295–3307.
LIBERZON, D. & SHEMER, L. 2011 Experimental study of the initial stages of wind waves' spatial evolution. *J. Fluid Mech.* **681**, 462–498.
LONGO, S., CHIAPPONI, L., CLAVERO, M., MÄKELÄ, T. & LIANG, D. 2012 Study of the turbulence in the air-side and water-side boundary layers in experimental laboratory wind induced surface waves. *Coast. Engng* **69**, 67–81.
MASSEL, S.R. 1996 *Ocean Surface Waves: Their Physics and Prediction*, vol. 11. World Scientific.
MELLOR, G.L. & GIBSON, D.M. 1966 Equilibrium turbulent boundary layers. *J. Fluid Mech.* **24** (2), 225–253.
MILES, J.W. 1957 On the velocity profile for turbulent flow near a smooth wall. *J. Aero. Sci.* **24**, 704.
MITSUYASU, H. 1969 Observations of the wind and waves at the hakata bay. *Bull. Res. Inst. Appl. Mech., Kyushu Univ., (in Japanese)* **33**, 33–66.
MITSUYASU, H. 1970 On the growth of the spectrum of wind-generated waves. *Coast. Engng Japan* **13**, 1–14.
MITSUYASU, H. & HONDA, T. 1974 The high frequency spectrum of wind-generated waves. *J. Oceanogr. Soc. Japan* **30**, 185–198.
MITSUYASU, H. & HONDA, T. 1982 Wind-induced growth of water waves. *J. Fluid Mech.* **123**, 425–442.
MITSUYASU, H. & RIKIISHI, K. 1978 The growth of duration-limited wind waves. *J. Fluid Mech.* **85** (4), 705–730.
NEUMANN, G. 1956 Wind stress on water surfaces. *Bull. Am. Meteorol. Soc.* **37** (5), 211–217.
NIKURADSE, J. 1950 Laws of flow in rough pipes (eng. transl.). *Tech. Rep.* 12. NACA Tech. Mem.
NUGROHO, B., MONTY, J.P., UTAMA, I.K.A.P., GANAPATHISUBRAMANI, B. & HUTCHINS, N. 2021 Non-k-type behaviour of roughness when in-plane wavelength approaches the boundary layer thickness. *J. Fluid Mech.* **911**, A1.

PEÑA, A. & GRYNING, S.E. 2008 Charnock's roughness length model and non-dimensional wind profiles over the sea. *Boundary-Layer Meteorol.* **128** (2), 191–203.

PICHUGINA, Y.L., BANTA, R.M., BREWER, W.A., SANDBERG, S.P. & HARDESTY, R.M. 2012 Doppler lidar–based wind-profile measurement system for offshore wind-energy and other marine boundary layer applications. *J. Appl. Meteorol. Climatol.* **51** (2), 327–349.

PLANT, W.J. & WRIGHT, J.W. 1977 Growth and equilibrium of short gravity waves in a wind-wave tank. *J. Fluid Mech.* **82** (4), 767–793.

PRANDTL, L. 1932 Meteorogische an wendung der stromungslehre. *Beitr. Phys. Atmos.* **19**, 188–202.

PRANDTL, L. & SCHLICHTING, H. 1934 Das widerstandsgesetz rauher platten. *Werft, Reederei, Hafen* **15** (1), 1–4.

RAUPACH, M.R., ANTONIA, R.A. & RAJAGOPALAN, S. 1991 Rough-wall boundary layers. *Appl. Mech. Rev.* **44**, 1–25.

SCHLICHTING, H. 1979 *Boundary-Layer Theory*. McGraw-Hill.

SCHULTZ, M.P. & FLACK, K.A. 2007 The rough-wall turbulent boundary layer from the hydraulically smooth to the fully rough regime. *J. Fluid Mech.* **580**, 381–405.

SHEMER, L. 2019 On evolution of young wind waves in time and space. *Atmosphere* **10** (9), 562.

SHEMER, L., SINGH, S. & CHERNYSHOVA, A. 2020 Spatial evolution of young wind waves: numerical modelling verified by experiments. *J. Fluid Mech.* **901**, A22.

SHEMER, L. & SINGH, S.K. 2021 Spatially evolving regular water wave under the action of steady wind forcing. *Phys. Rev. Fluids* **6** (3), 034802.

SHOCKLING, M.A., ALLEN, J.J. & SMITS, A.J. 2006 Roughness effects in turbulent pipe flow. *J. Fluid Mech.* **564**, 267–285.

SMITH, S.D. 1980 Wind stress and heat flux over the ocean in gale force winds. *J. Phys. Oceanogr.* **10** (5), 709–726.

SRIDHAR, A., PULLIN, D.I. & CHENG, W. 2017 Rough-wall turbulent boundary layers with constant skin friction. *J. Fluid Mech.* **818**, 26–45.

TALLURU, K.M., DJENIDI, L., KAMRUZZAMAN, M.D. & ANTONIA, R.A. 2016 Self-preservation in a zero pressure gradient rough-wall turbulent boundary layer. *J. Fluid Mech.* **788**, 57–69.

TAYLOR, P.K. & YELLAND, M.J. 2001 The dependence of sea surface roughness on the height and steepness of the waves. *J. Phys. Oceanogr.* **31** (2), 572–590.

TOBA, Y. 1988 Similarity laws of the wind wave and the coupling process of the air and water turbulent boundary layers. *Fluid Dyn. Res.* **2** (4), 263–279.

TOBA, Y., IIDA, N., KAWAMURA, H., EBUCHI, N. & JONES, I.S.F. 1990 Wave dependence of sea-surface wind stress. *J. Phys. Oceanogr.* **20** (5), 705–721.

TOBA, Y., SMITH, D. & EBUCHI, N. 2001 Wind stress over the ocean. In *Historical Drag Expressions* (ed. I.S.F. Jones). Cambridge University Press.

TSENG, R.S, HSU, Y.H.L. & WU, J. 1992 Methods of measuring wind stress over a water surface — discussions of displacement height and von Karman constant. *Boundary-Layer Meteorol.* **58** (1), 51–68.

WHITE, F.M. 2006 *Viscous Fluid Flow*. McGraw-Hill.

WU, J. 1969 Wind stress and urface roughness at air-sea interface. *J. Geophys. Res.* **74**, 444–455.

YOUNG, I.R. 1999 *Wind Generated Ocean Waves*. Elsevier.

ZAVADSKY, A., BENETAZZO, A. & SHEMER, L. 2017 Study of spatial variability of short gravity waves in a wind wave tank by optical methods. *Phys. Fluids* **29**, 016601.

ZAVADSKY, A., LIBERZON, D. & SHEMER, L. 2013 Statistical analysis of the spatial evolution of the stationary wind wave field. *J. Phys. Oceanogr.* **43** (1), 65–79.

ZAVADSKY, A. & SHEMER, L. 2012 Characterization of turbulent airflow over evolving water-waves in a wind-wave tank. *J. Geophys. Res.* **117**, C00J19.

ZAVADSKY, A. & SHEMER, L. 2017*a* Investigation of statistical parameters of the evolving wind wave field using a laser slope gauge. *Phys. Fluids* **29**, 056602.

ZAVADSKY, A. & SHEMER, L. 2017*b* Water waves excited by near-impulsive wind forcing. *J. Fluid Mech.* **828**, 459–495.